ACS APPLIED ELECTRONIC MATERIALS

pubs.acs.org/acsaelm Article

Correlation between Structural Studies and the Cathodoluminescence of Individual Complex Niobate Particles

Rasa Changizi, Siyuan Zhang, Christian Ziegler, Torsten Schwarz, Bettina V. Lotsch, and Christina Scheu*

Cite This: ACS Appl. Electron. Mater. 2021, 3, 461−467

Read Online

ACCESS | Metrics & More | Article Recommendations

ABSTRACT: Lanthanide-doped semiconductors and the mechanism of energy transfer from host to lanthanide ions have always been a topic of great interest. In this study, we underline the effect of the lanthanide ions' surroundings on the width of the emission lines. We show that different crystal structures and lattice defects within the crystal lead to different atomic coordinates of the ion. In this work, complex niobates synthesized in a solid-state route were investigated. Because of the micron size of the particles, scanning electron microscopy in addition to energy dispersive X-ray spectroscopy were used to study the morphology and chemical composition, respectively. Moreover, the correlation between chemical composition and the crystal structure of the particles was investigated using transmission electron microscopy. These analyses show the presence of two phases with different chemical compositions and crystal structures, namely $PrNbO_4$ and Pr^{3+}:$Ca_2Nb_2O_7$. We studied the optical properties of both phases using a cathodoluminescence spectrometer attached to the scanning electron microscope. In the cathodoluminescence spectra of $PrNbO_4$, that is, for particles with higher Pr content, brighter emission lines were observed. Possible causes for the improved luminescent properties of $PrNbO_4$ are the higher amounts of Pr as both K and Ca atoms are substituted in the initial $KCa_2Nb_3O_{10}$ powder by Pr; therefore, Pr^{3+} ions are surrounded by Nb and O only. As a result, Pr^{3+} ions occupy the sites with C_2 symmetry, which helps remove the parity forbidden f−f transitions.

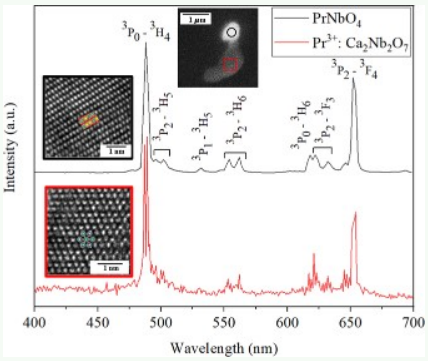

KEYWORDS: *lanthanides, trivalent praseodymium, complex niobates, cathodoluminescence, spectroscopy, correlative microscopy, transmission electron microscopy*

1. INTRODUCTION

Trivalent lanthanides (Ln^{3+}) have a specific configuration of inner shell 4f orbitals, from which electronic transitions arise. As the 4f orbital is very well shielded from any coupling with other ligands by the outer filled 5s and 5p orbitals, these materials have magnetic and optical properties.[1,2] Laporte rule states that f−f transitions are forbidden; however, according to the crystal field theory, due to the influence of the coordination geometrical symmetry around the lanthanide ion, these transitions become partially allowed.[3] The Judd-Ofelt theory explains how the crystal field perturbates the orbitals of the lanthanide ion. This perturbation causes mixing of the orbitals with different parities, and as a result, the forbidden f−f transition become partially allowed.[4−6] To achieve emission spectra with high intensity and sharp emission lines, different factors such as doping concentration, the ionic radii mismatch to the host, and different lattice sites for the lanthanide ions have been investigated.[7,8] Morais Faustino et al.[8] have shown that increasing the doping concentration of Eu^{3+} to a certain amount optimizes the emission intensity. However, increasing the concentration more than the optimum amount leads to emission quenching, which is caused by nonradiative energy transfer between Eu^{3+} ions. The optimum concentration of Eu^{3+} dopants changes remarkably with the type of host material, synthesis conditions, etc.[8] Furthermore, the authors suggest that due to the mismatch of ionic radii, the doping mechanisms play a crucial role for the formation of defects within the host. In another work, Krishnan and Swart studied the influence of different doping concentrations on the cathodoluminescence (CL) properties of a series of monoclinic phase $BaY_2(MoO_4)_4$ phosphor powders doped with Eu^{3+}.[9] They have concluded that not only by increasing the doping content but also with a deeper penetration depth of the incident electrons, the CL intensity increases linearly.[9,10]

During the past few years, several studies have been done on different lanthanides doped into various hosts.[2,11−20] Great

Received: November 14, 2020
Accepted: January 4, 2021
Published: January 13, 2021

attention has been paid to oxide-based materials doped with Ln^{3+}.[21,22] Nico et al.[11] have suggested to use niobates as the host. Commonly, rare earth (RE) niobates have been considered as host matrices and have also attracted interests as potential rare earth-doped laser hosts.[7] The $RENbO_4$ phases are known to crystallize in a fergusonite-type crystal structure, that is, in a monoclinic crystal structure.[11]

Many applications for the lanthanide-doped materials in the field of optoelectronic devices such as LEDs, lasers, and optical amplifiers have been suggested.[12,21,23,24] Lanthanide-doped niobates are interesting materials in the field of photorefractive memories and as linear and self-frequency converter solid state laser materials.[7,13,25]

Although there exist many studies on lanthanide-doped oxides, it is interesting that, to our knowledge, no report has been published that deals with correlating optical, structural, and chemical properties. Even studies with CL lack this correlation. Pr^{3+} has attracted a lot of attention due to its efficiency of emitting photons from the UV to infrared (IR) spectral regions.[17] There are also versatile applications for lanthanide-doped niobates.[7,13,25] Therefore, in the present study, we demonstrate for Pr^{3+}-doped niobate powders the importance to study individual particles. Their crystal structure and chemical composition are investigated by electron microscopy, and the results are correlated with their optical properties measured by CL.

2. EXPERIMENTAL SECTION

2.1. Preparation of Complex Niobates Powder. Pr^{3+}-doped $KCa_2Nb_3O_{10}$ were synthesized in a solid-state route according to protocols modified from those reported in the literature.[26] For preparation of Pr^{3+}-doped oxides, desired amounts of K_2CO_3, $CaCO_3$, and Nb_2O_5 were mixed together with Pr_6O_{11}. This mixture was then grinded and heated to temperatures between 1100 and 1300 °C. After all products were washed in deionized water, they were dried at room temperature. Then 20 at% excess of K_2CO_3 and $CaCO_3$ was added to the compounds to compensate for evaporation losses during heating. Pr with high amount of concentration $[x = 0.75]$ was doped into $KCa_2Nb_3O_{10}$ particles to reach the nominal formula $Pr_xK_{1-x}Ca_{2-x}Nb_3O_{10}$. However, later characterization determined that this was not the case and instead, complex niobates were produced as a result of this reaction.

2.2. Characterization. X-ray diffraction (XRD) data of powders were collected using a Huber G670 Guinier imaging plate diffractometer (Huber, Rimsting; Cu $K_{\alpha 1}$ radiation, λ = 154.051 pm, Ge (111)-monochromator). The particle morphology was analyzed by an Auriga Zeiss SEM equipped with an in-lens detector and coupled with energy dispersive X-ray spectroscopy (EDX) for composition analysis. Elemental quantification was done using the ZAF quantification method by the Team software. Secondary electron images and EDX data were acquired at 10 keV. CL data were recorded using FEI Helios Nanolab 600 equipped with a paraboloidal mirror, MonoCL4 monochromator (acquisition software Gatan DigitalMicrograph), and a liquid N_2 cooled Hamamatsu photomultiplier tube R5509−73. The sample powders were irradiated with an electron beam of 10 keV and beam current of 5.5 nA. Furthermore, crystal structure analysis of individual particles was done using a Thermo Fisher Scientific Titan transmission electron microscope (TEM) operated at 300 kV, equipped with an X-FEG (field emission gun) as electron source and an aberration corrector for the objective lens. For SEM investigations, the powder was dispersed on a Si substrate, while for TEM an Au-finder grid coated with a continuous carbon film was used.

3. RESULTS AND DISCUSSION

3.1. EDX and XRD Data of Powder. EDX measurements of powder show Ca, Pr, Nb, and O with the corresponding average composition 5.3 at%, 5.9 at%, 10.3 at%, and 78.4 at%. The values are average values of three EDX measurements taken over a size of several-hundred microns. No K was detected. This indicates that K is evaporated and not incorporated into the lattice for such a high amount of Pr. Figure 1 compares the XRD patterns of the pure $KCa_2Nb_3O_{10}$ powder[26] with the Pr^{3+}-doped compounds.

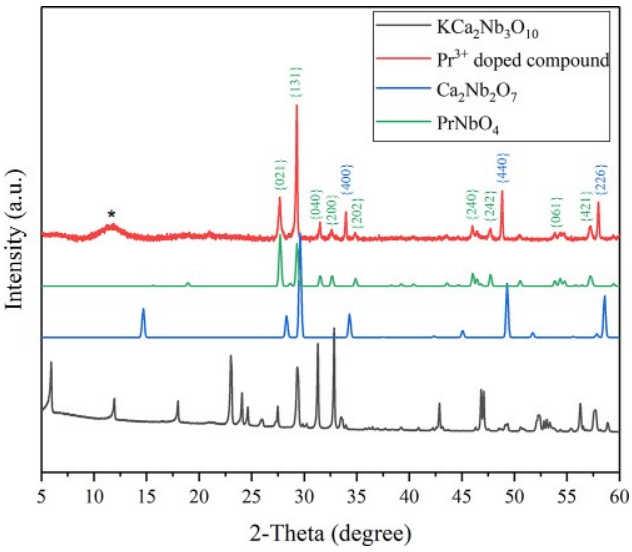

Figure 1. XRD pattern of Pr^{3+}-doped compound (red curve) in comparison with the reference $KCa_2Nb_3O_{10}$ (black curve); $Ca_2Nb_2O_7$ [ICSD 72206] is shown in blue and $PrNbO_4$ [ICSD 109176] is indicated in green. ∗ indicates an instrumental artifact.

The XRD pattern of the synthesized Pr-doped material (red pattern in Figure 1) does not fit to the monoclinic crystal structure of $KCa_2Nb_3O_{10}$, as only a few reflections occur at similar 2θ values. Instead all reflections can be explained by the presence of two other phases. One is $PrNbO_4$, which has also a monoclinic crystal structure (space group: $C2/c$) with lattice parameters a = 5.499 Å, b = 5.157 Å, c = 11.342 Å, and $\alpha = 90°$, $\beta = 94.57°$, $\gamma = 90°$ (ICSD 109176). The reference pattern is shown in green in Figure 1. The peaks at $2\theta = 33.95°$, 48.9°, and 57.96° do not belong to $PrNbO_4$ but match to the cubic crystal structure of $Ca_2Nb_2O_7$(ICSD 72206). The pure, cubic $Ca_2Nb_2O_7$ (space group: $Fd\bar{3}m$) has a lattice parameter a = 10.445 Å. The reference pattern of this phase is displayed in blue in Figure 1 and shows slightly shifted peaks at $2\theta = 34.31°$, 49.31°, and 58.55°. Other peaks of this phase partly overlap with the one of the $PrNbO_4$ phase. The peaks that are slightly shifted to lower 2θ values indicate an increase in the interplanar spacing. In this coordination geometry, ionic radii of Ca and Nb are 1.12 and 0.64 Å, respectively. When Nb is replaced by Pr, the ionic radius changes to 0.99 Å. Therefore, the increase in the interplanar spacing is most likely due to the Pr ions sitting on Nb sites within the $Ca_2Nb_2O_7$ crystal lattice, for example, a Pr-doped $Ca_2Nb_2O_7$ (Pr^{3+}:$Ca_2Nb_2O_7$) phase has formed. We have calculated this crystal lattice strain, which is 0.5%. The XRD results thus indicate that during the synthesis, two phases were formed.

It is worth mentioning here that according to ref 8, multiple sites exist in the lattice of lanthanide-doped materials, which were studied by the visible emission bands of the Ln^{3+}. For example, after investigating the local structure around the Ln^{3+}

https://dx.doi.org/10.1021/acsaelm.0c01003
ACS Appl. Electron. Mater. 2021, 3, 461−467

dopants, it was found that Ln^{3+} ions enter the $ABNbO_3$ structure with A and B being alkali and alkaline earth metals not only by substituting A and B but also by substituting Nb lattice positions.[7] Similarly, in our sample, not only the K of $KCa_2Nb_3O_{10}$ is completely replaced but also Ca and Nb are partly replaced by Pr.

3.2. Elemental Analysis (EDX) of Individual Particles. As the XRD data indicated the presences of two phases, Pr^{3+}:$Ca_2Nb_2O_7$ and $PrNbO_4$, it was important to obtain EDX data of individual particles to correlate the chemical composition and the corresponding CL spectrum. The EDX spectra for two selected particles are shown in Figure 2, together with their SEM image. The particles are micron-sized. The EDX spectra proved the presence of Si, O, Nb, Ca, and Pr. In accordance to the EDX measurements over the powder, no K is detected. Since low energy peaks, such as the O–K_α line, cannot be quantified precisely due to the high amount of absorption by the specimen, O in addition to Si (from the substrate) and other contaminations such as F were removed from the quantification. The higher intensity of the Si–K_α line in Figure 2a is due to larger contributions from the substrate as the particle is thinner in this region. EDX was performed for 21 single particles. Regarding their chemical composition, both phases were found in these particles. In phase (i) for 13 particles, the elements Ca, Nb, and Pr were observed with the corresponding average composition of 37.5 at%, 39.7 at%, and 22.8 at% besides O.

By plotting the concentrations of Ca and Nb against the Pr concentration, a linear dependency was found (see Figure 3). As a result, with a good approximation, the chemical formula was obtained as $Pr_xCa_{48-x/2}Nb_{52-x/2}O_y$, the average composition of x equals to 20 at%. In phase (ii) for 8 particles, only Pr and Nb with almost constant composition of (46.4 at% for Nb and 53.6 at% for Pr) were found besides O. Comparing the ratio of Pr and Nb with the stoichiometric ratio, that is, Pr:Nb = 1:1, it indicates that a small fraction of the Pr ions are located on Nb sites within the $PrNbO_4$ crystal structure.

Comparing the Pr concentration in both phases, a higher amount of Pr is found in the second phase where both Ca and K atoms are substituted by Pr. As a result, Pr is replacing K and is substituting also locally Ca and Nb. Since the measured concentrations of Pr are higher than its solubility limit in Pr^{3+}-doped $KCa_2Nb_3O_{10}$, the aforementioned two phases are formed during annealing. Several SEM images at different magnifications were taken of each particle. This made it possible to trace back and identify all the 21 single particles in the microscope where we did the CL measurements.

3.3. CL Properties of $PrNbO_4$ and Pr^{3+}:$Ca_2Nb_2O_7$. To study the optical properties of the two formed phases, that is, $PrNbO_4$ and Pr^{3+}:$Ca_2Nb_2O_7$, CL measurements of single particles were obtained. A representative CL spectrum of $PrNbO_4$ is plotted in Figure 4 in black, which exhibits the following transitions $^3P_0$ to $^3H_4$, $^3P_2$ to $^3H_5$, $^3P_1$ to $^3H_5$, $^3P_2$ to $^3H_6$,$^3P_0$ to $^3H_6$, $^3P_2$ to $^3F_3$,$^3P_0$ to$^3F_2$, and $^3P_2$ to $^3F_4$. Spectra of

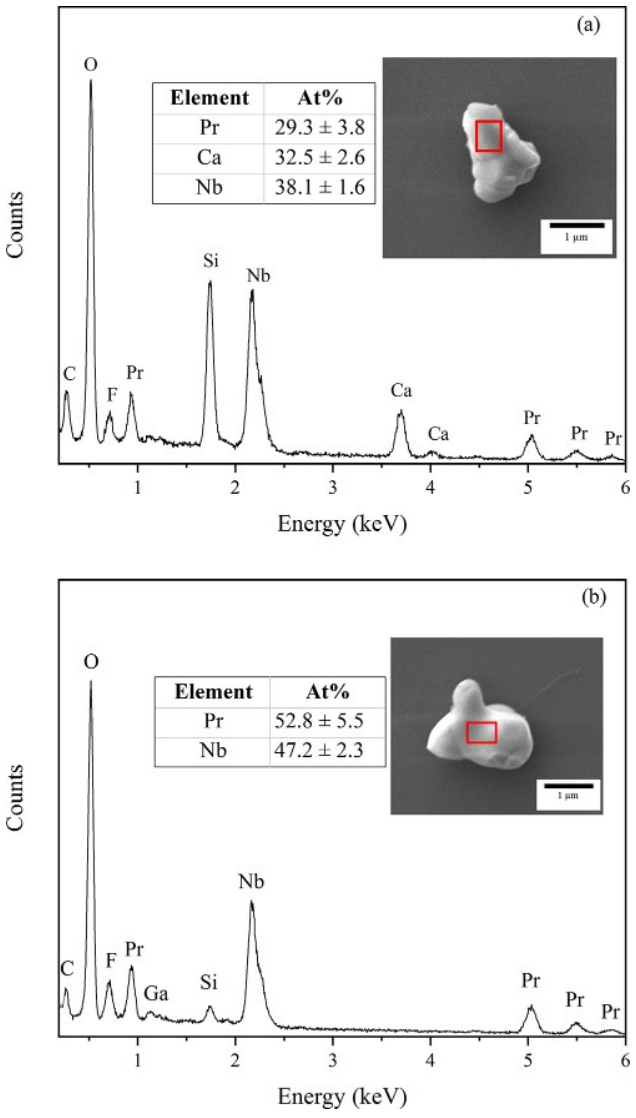

Figure 2. Energy dispersive X-ray spectra of individual (a) Pr^{3+}:$Ca_2Nb_2O_7$ and (b) $PrNbO_4$ particles. The area where the data were acquired is indicated by a red box in the SEM image shown as inset.

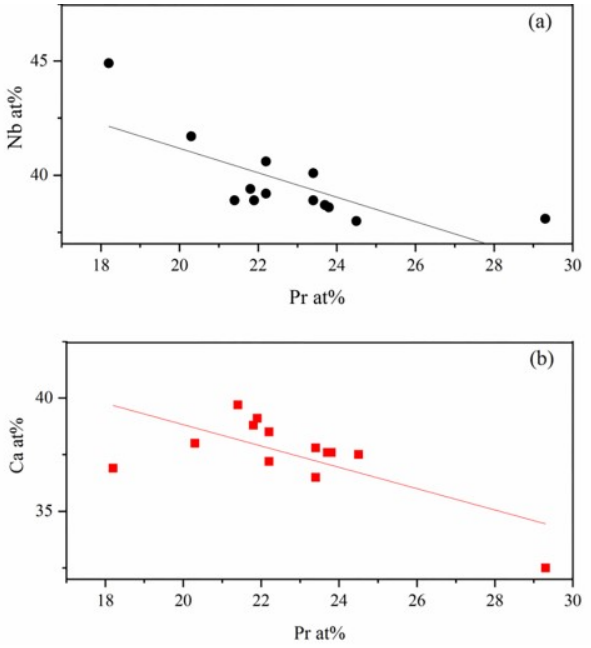

Figure 3. Pr at% versus (a) Nb at% and (b) Ca at% for a set of individual nanoparticles with the formula $Pr_xCa_{48-x/2}Nb_{52-x/2}O_y$.

https://dx.doi.org/10.1021/acsaelm.0c01003
ACS Appl. Electron. Mater. 2021, 3, 461–467

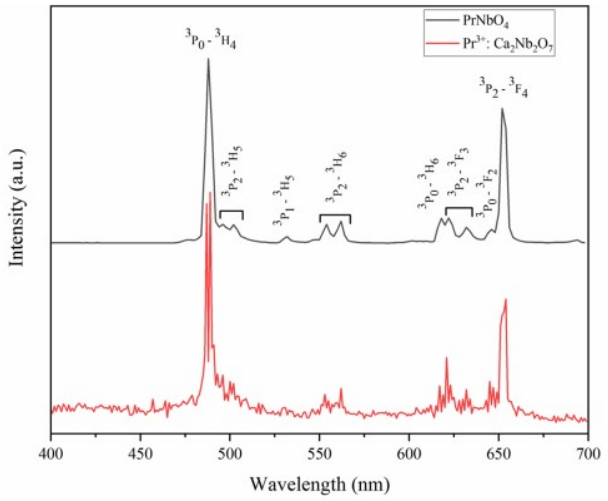

Figure 4. CL spectra of $PrNbO_4$ (black curve) and Pr^{3+}:$Ca_2Nb_2O_7$ (red curve).

particles with the formula Pr^{3+}:$Ca_2Nb_2O_7$ were also acquired. The red curve in Figure 4 shows one representative CL spectrum with major emission lines (higher than the noise level), which can be associated with the $^3P_0$ to $^3H_4$, $^3P_2$ to $^3H_6$, $^3P_0$ to $^3H_6$, $^3P_2$ to $^3F_3$, $^3P_0$ to $^3F_2$, and $^3P_2$ to $^3F_4$ electric dipole transitions of Pr^{3+}. All transitions were labeled according to the Dieke diagram (Pr^{3+}:$LaCl_3$).[27] In comparison with the Dieke diagram, our emission lines deviate by less than ±4 nm (see Table 1).

The wavelengths of each emission line are listed in Table 1. The strongest emission lines belong to $^3P_0$ to $^3H_4$ and $^3P_2$ to $^3F_4$ transitions, which are at 489 and 653 nm, respectively, in both phases. Similar main emission lines were reported for other Pr^{3+}-doped systems.[25,28,29] Both phases show the identical wavelength values for each transition. However, the transitions belonging to $^3P_2$ to $^3H_5$ and $^3P_1$ to $^3H_5$ were not clear in Figure 4 for the Pr^{3+}:$Ca_2Nb_2O_7$ phase as the related emission peaks show low intensity.

We normalized the CL spectra to their highest peak ($^3P_0$ to $^3H_4$) to 100, and the relative intensities for the other transitions are given in Table 2. In the spectra of $PrNbO_4$, the intensity ratio between the dominant transitions ($^3P_0$ to $^3H_4$ and $^3P_2$ to $^3F_4$) is lower than for the other phase. However, the intensity ratios between the emission line originating from $^3P_0$ to $^3H_4$ and the remaining emissions are higher for $PrNbO_4$ compared to the one of the Pr^{3+}:$Ca_2Nb_2O_7$ spectrum.

On the basis of our CL results, we can conclude that for each phase ($PrNbO_4$ and Pr^{3+}:$Ca_2Nb_2O_7$), depending on Pr concentration and which host element it is substituting, similar transition peaks but varying intensity ratios can be found. Depending on which site Ln^{3+} ions occupy, different transitions can be achieved.[30−33] If the active ions occupy the site with C_2 symmetry (RE sites), which leads to the removal of the parity-forbidden f−f transition, a higher intensity can be observed.[13] Magnetic-dipole transitions are independent of site symmetry, whereas electric-dipole ones are only allowed at sites of low symmetry with no inversion center.[8] Therefore, the high intensity of some peaks indicates that a significant proportion of the Pr^{3+} is located in noncentrosymmetric sites, whereas broad emission lines are related to the lower incorporation of Pr^{3+} ions into the crystal lattice.[8]

Table 2. Intensity Comparison between Both Spectra[a]

formula	$^3P_0$ to $^3H_4$	$^3P_2$ to $^3H_5$	$^3P_1$ to $^3H_5$	$^3P_2$ to $^3H_6$	$^3P_0$ to $^3H_6$	$^3P_2$ to $^3F_3$	$^3P_0$ to $^3F_2$	$^3P_2$ to $^3F_4$
Pr^{3+}:$Ca_2Nb_2O_7$	100	-	-	16	19	30	21	55
				19		18		
$PrNbO_4$	100	11	3	11	15	15	8	65
		11		12		9		

[a]All wavelengths are in nm.

3.4. Crystal Structure Analysis. To confirm that the luminescent properties of $PrNbO_4$ are due to its chemistry and crystal structure, TEM measurements were performed on these particles. Figure 5a shows a bright field TEM image of a $PrNbO_4$ particle. Since the particle thickness was very thin at the edges, the high-resolution TEM (HRTEM) image (see Figure 5b) was taken on this area. The corresponding selected area electron diffraction (SAED) pattern is shown Figure 5c. The crystal was oriented in the $[2\bar{3}0]$ zone axis, and for the corresponding SAED pattern we indexed the (002) and (321) and $(32\bar{1})$ planes. Furthermore, we identified for the particle a monoclinic structure, which agrees well with the one for $PrNbO_4$ (ICSD 109176). The same crystal structure is reported for several lanthanide-doped niobate systems.[11,13,34]

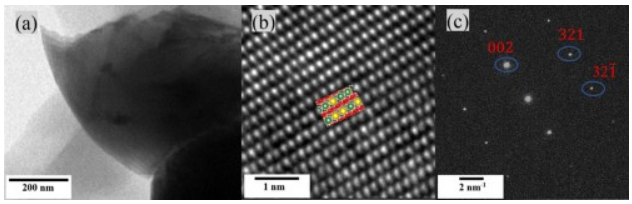

Figure 5. (a) TEM of an individual particle, (b) HRTEM image; (green spheres, niobium; yellow, praseodymium; red, oxygen) and (c) corresponding SAED patterns of $PrNbO_4$ in the $[2\bar{3}0]$ zone axis.

The structure of $PrNbO_4$ in its monoclinic structure viewed along $[2\bar{3}0]$ is superimposed in Figure 5b using the program VESTA ver. 3.3.2 and basic atom locations: Pr(0.25, 0.12, 0), Nb(0.25, 0.65, 0), and O(0.01, 0.72, 0.2). The crystal structure of $PrNbO_4$ is depicted in Figure 6. As shown on the figure, Pr is bonded to eight O atoms in a 8-coordinate geometry (maximum

Table 1. Wavelength Comparison between Both Spectra and the Dieke Diagram (Pr^{3+}:$LaCl_3$)[a]

formula	$^3P_0$ to $^3H_4$	$^3P_2$ to $^3H_5$	$^3P_1$ to $^3H_5$	$^3P_2$ to $^3H_6$	$^3P_0$ to $^3H_6$	$^3P_2$ to $^3F_3$	$^3P_0$ to $^3F_2$	$^3P_2$ to $^3F_4$
Pr^{3+}: $Ca_2Nb_2O_7$	489	low SNR[b]	low SNR[b]	553 562	617	621 632	645	653
$PrNbO_4$	489	495 502	531	553 562	617	621 632	645	653
Pr^{3+}: $LaCl_3$	492	500	531	558	617	625	645	649

[a]All wavelengths are in nm. [b]SNR stands for signal-to-noise ratio.

https://dx.doi.org/10.1021/acsaelm.0c01003
ACS Appl. Electron. Mater. 2021, 3, 461−467

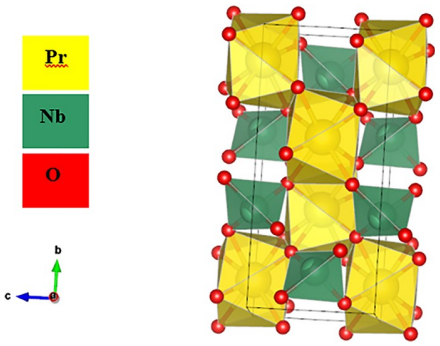

Figure 6. Crystal structure of $PrNbO_4$.

bond length: 2.74 Å). Nb in a tetrahedral geometry is bonded to four O atoms (maximum bond length: 2.45 Å).

Figure 7a shows the BF TEM image of the Pr^{3+}:$Ca_2Nb_2O_7$. In Figure 7b, a HRTEM image of the particle taken in the [111]

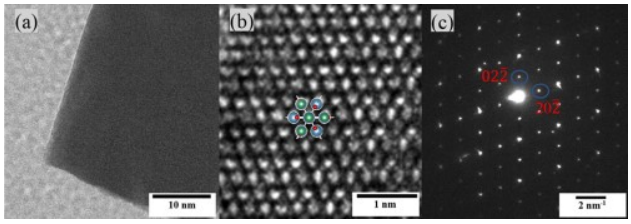

Figure 7. (a) TEM, (b) HRTEM image (blue spheres, calcium; green, niobium; red, oxygen), and (c) corresponding SAED patterns of the Pr^{3+}:$Ca_2Nb_2O_7$ phase in the [111] zone axis.

zone axis is shown. The corresponding SAED pattern of this particle is given in Figure 7c. The diffraction patterns index well to the one for $Ca_2Nb_2O_7$ (ICSD 72206). VESTA was used to show the structure of $Ca_2Nb_2O_7$ and the zone [111], which is superimposed in Figure 7b. The following basic atom locations were used: Ca(0.5, 0.5, 0.5), Nb(0, 0, 0), and O(0.32, 0.12, 0.12).

Figure 8 illustrates the crystal structure of $Ca_2Nb_2O_7$. Ca is bonded to eight O atoms and forms a distorted CaO_8 hexagonal

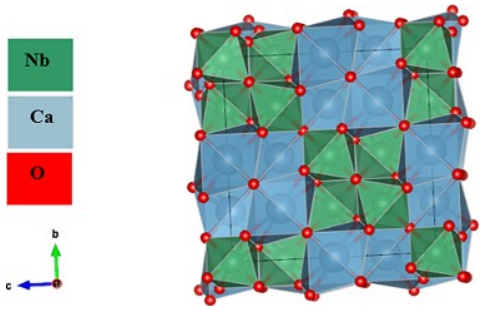

Figure 8. Crystal structure of $Ca_2Nb_2O_7$.

bipyramids (maximum bond length: 2.83 Å). Nb is bonded to six equivalent O atoms to form NbO_6 octahedra (maximum bond length: 2.45 Å). In case of Pr^{3+}:$Ca_2Nb_2O_7$ particles, Pr^{3+} occupies Ca (16d) and Nb (16c) sites. To compensate for charge neutrality, Ca vacancies can form close to Pr(Ca) sites and O vacancies can form around Pr(Nb) sites, similar to the mechanism described by Górecka et al.[35] for Eu^{3+}-doped $Ca_9Y(PO_4)_7$.

We have measured the *d* spacing value corresponding to the (111) plane based on the diffraction pattern of a Pr^{3+}:$Ca_2Nb_2O_7$ particle. The *d* spacing in this case is 6.4 Å. According to ICSD 72206, the *d* value for the same plane of $Ca_2Nb_2O_7$ is 6.03 Å. Because of the difference that exists between these values, the chemical formula calculated for this phase and obtaining two different CL spectra for each phase, we assume that Pr should be sitting on Ca and Nb sites almost equally.

4. CONCLUSION

Pr^{3+}-doped $KCa_2Nb_3O_{10}$ was synthesized via a solid-state route. Complex niobates with different phases, namely, $PrNbO_4$ and Pr^{3+}:$Ca_2Nb_2O_7$, were produced during the annealing process. Characterization of both phases was achieved by XRD, EDX, CL, and TEM analysis. The main conclusions drawn from this study are summarized as follows.

1. XRD patterns of Pr^{3+}-doped compounds index well to the monoclinic crystal structure of $PrNbO_4$ and the cubic crystal structure of $Ca_2Nb_2O_7$. There is a small shift in the XRD pattern of Pr-doped compounds compared to the one for $Ca_2Nb_2O_7$, which indicates an increase in the *d* spacing value. This confirms that Pr ions with bigger ionic radius value must occupy Nb sites.
2. In the SEM, individual micron-sized particles were observed. EDX results show the presence of both phases. On the basis of these data, chemical formulas of the phases were calculated. In $PrNbO_4$, a higher amount of Pr with the average of 53.6 at% is found as a result of both Ca and K atoms being substituted by Pr. In Pr^{3+}:$Ca_2Nb_2O_7$, Pr ions occupy both Ca and Nb sites almost equally. Average Pr content in this phase is 22.8 at%.
3. The CL data show similar transition lines but varying intensity ratios for $PrNbO_4$ and Pr^{3+}:$Ca_2Nb_2O_7$. In the spectrum of $PrNbO_4$, brighter emission lines exist compared to the ones from the second phase. This is due to the fact that more Pr atoms are occupying sites with C_2 symmetry, which leads to the removal of the parity-forbidden f−f transition. In both spectra, major emission lines are labeled in which the dominant ones are associated with the $^3P_0$ to $^3H_4$ and $^3P_2$ to $^3F_4$ of electric dipole transition of Pr.
4. Both phases, $PrNbO_4$ and Pr^{3+}:$Ca_2Nb_2O_7$, are observed and characterized by TEM. Monoclinic crystal structure for $PrNbO_4$ and cubic structure for Pr^{3+}:$Ca_2Nb_2O_7$ were observed based on the diffraction pattern for each phase and comparison with ICSD data of $PrNbO_4$ and $Ca_2Nb_2O_7$.

On the basis of these results, lanthanide-doped niobates with brighter emission lines are better candidates in terms of luminescent efficiency and can be used in various applications.

AUTHOR INFORMATION

Corresponding Author

Christina Scheu − *Max-Planck-Institut für Eisenforschung GmbH, 40237 Düsseldorf, Germany;* orcid.org/0000-0001-7916-1533; Email: scheu@mpie.de

Authors

Rasa Changizi − *Max-Planck-Institut für Eisenforschung GmbH, 40237 Düsseldorf, Germany*

https://dx.doi.org/10.1021/acsaelm.0c01003
ACS Appl. Electron. Mater. 2021, 3, 461−467

Siyuan Zhang − *Max-Planck-Institut für Eisenforschung GmbH, 40237 Düsseldorf, Germany;* orcid.org/0000-0001-7045-0865
Christian Ziegler − *Department of Chemistry, Ludwig Maximilian University of Munich, 81377 München, Germany*
Torsten Schwarz − *Max-Planck-Institut für Eisenforschung GmbH, 40237 Düsseldorf, Germany*
Bettina V. Lotsch − *Department of Chemistry, Ludwig Maximilian University of Munich, 81377 München, Germany; Max Planck Institute for Solid State Research, 70569 Stuttgart, Germany;* orcid.org/0000-0002-3094-303X

Complete contact information is available at: https://pubs.acs.org/10.1021/acsaelm.0c01003

Notes

The authors declare no competing financial interest.

■ ACKNOWLEDGMENTS

The authors thank Jörg Thomas and Philipp Watermeyer for the expert TEM technical assistance.

■ REFERENCES

(1) Hu, M.; Liu, W. Application of lanthanide-doped luminescence nanoparticles in imaging and therapeutics. In *Photonanotechnology for Therapeutics and Imaging*; Elsevier, 2020; pp 205−241.
(2) Wang, S.; Wang, L. Lanthanide-doped nanomaterials for luminescence detection and imaging. *TrAC, Trends Anal. Chem.* **2014**, *62*, 123−134.
(3) Kittel, C.; McEuen, P.; McEuen, P. *Introduction to solid state physics*; Wiley New York, 1996; Vol. *8*.
(4) Ferreira da Rosa, P. P.; Kitagawa, Y.; Hasegawa, Y. Luminescent lanthanide complex with seven-coordination geometry. *Coord. Chem. Rev.* **2020**, *406*, 213153.
(5) Hehlen, M. P.; Brik, M. G.; Krämer, K. W. 50th anniversary of the Judd-Ofelt theory: An experimentalist's view of the formalism and its application. *J. Lumin.* **2013**, *136*, 221−239.
(6) Walsh, B. M. Judd-Ofelt theory: principles and practices. In *Advances in spectroscopy for lasers and sensing*; Springer, 2006; pp 403−433.
(7) Pin, S.; Piccinelli, F.; Kumar, K. U.; Enzo, S.; Ghigna, P.; Cannas, C.; Musinu, A.; Mariotto, G.; Bettinelli, M.; Speghini, A. Structural investigation and luminescence of nanocrystalline lanthanide doped $NaNbO_3$ and $Na_{0.5}K_{0.5}NbO_3$. *J. Solid State Chem.* **2012**, *196*, 1−10.
(8) Morais Faustino, B. M.; Foot, P. J. S.; Kresinski, R. A. Lanthanide luminescence sensitization via SnO_2 nanoparticle host energy transfer. *J. Lumin.* **2019**, *206*, 205−210.
(9) Krishnan, R.; Swart, H. C. Cathodoluminescence properties of monoclinic phased reddish-orange emitting $BaY_2(MoO_4)_4$: Eu^{3+} phosphor. *Opt. Mater.* **2020**, *99*, 109604.
(10) Chen, H.; Wang, Y. Photoluminescence and cathodoluminescence properties of novel rare-earth free narrow-band bright green-emitting ZnB_2O_4: Mn^{2+} phosphor for LEDs and FEDs. *Chem. Eng. J.* **2019**, *361*, 314−321.
(11) Nico, C.; Monteiro, T.; Graça, M. P. Niobium oxides and niobates physical properties: Review and prospects. *Prog. Mater. Sci.* **2016**, *80*, 1−37.
(12) Dzierzgowski, K.; Wachowski, S.; Gojtowska, W.; Lewandowska, I.; Jasiński, P.; Gazda, M.; Mielewczyk-Gryń, A. Praseodymium substituted lanthanum orthoniobate: Electrical and structural properties. *Ceram. Int.* **2018**, *44* (7), 8210−8215.
(13) Dou, R.; Zhang, Q.; Gao, J.; Chen, Y.; Ding, S.; Peng, F.; Liu, W.; Sun, D. Rare-earth tantalates and niobates single crystals: Promising scintillators and laser materials. *Crystals* **2018**, *8* (2), 55.
(14) Vendrell, X.; García, J.; Cerdeiras, E.; Ochoa, D.; Rubio-Marcos, F.; Fernández, J.; Mestres, L. Effect of lanthanide doping on structural, microstructural and functional properties of $K_{0.5}Na_{0.5}NbO_3$ lead-free piezoceramics. *Ceram. Int.* **2016**, *42* (15), 17530−17538.
(15) Lorenz, K.; Nogales, E.; Miranda, S.; Franco, N.; Méndez, B.; Alves, E.; Tourbot, G.; Daudin, B. Enhanced red emission from praseodymium-doped GaN nanowires by defect engineering. *Acta Mater.* **2013**, *61* (9), 3278−3284.
(16) Bizeto, M. A.; Constantino, V. R.; Brito, H. F. Luminescence properties of the layered niobate $KCa_2Nb_3O_{10}$ doped with Eu^{3+} and La^{3+} ions. *J. Alloys Compd.* **2000**, *311* (2), 159−168.
(17) Mhlongo, G.; Dhlamini, M. S.; Ntwaeaborwa, O.; Swart, H.; Hillie, K. Luminescent properties and quenching effects of Pr^{3+} co-doping in SiO_2: Tb^{3+}/Eu^{3+} nanophosphors. *Opt. Mater.* **2014**, *36* (4), 732−739.
(18) Adell, I.; Solé, R. M.; Pujol, M. C.; Aguiló, M.; Díaz, F. Optimization of the Synthesis and Physical Characterization of Praseodymium-Doped Type III KGd $(PO_3)_4$ Nanocrystals. *ACS omega* **2018**, *3* (9), 11307−11316.
(19) Shi, Y.; Quan, B.; Ning, Q.; Cao, S.; Shi, J.; Dong, C. Photoluminescent properties and Judd-Ofelt analysis of novel $Na_{0.5}Sr_{0.25}NbO_3$: Eu^{3+} red phosphor with high quantum efficiency. *Mater. Res. Bull.* **2018**, *101*, 363−370.
(20) Macalik, L.; Maczka, M.; Hanuza, J.; Godlewska, P.; Solarz, P.; Ryba-Romanowski, W.; Kaminskii, A. Spectroscopic properties of the CaNb2O6: Pr^{3+} single crystal. *J. Alloys Compd.* **2008**, *451* (1−2), 232−235.
(21) Diallo, P.; Jeanlouis, K.; Boutinaud, P.; Mahiou, R.; Cousseins, J. Improvement of the optical performances of Pr^{3+} in $CaTiO_3$. *J. Alloys Compd.* **2001**, *323*, 218−222.
(22) Pan, G.; Bai, X.; Yang, D.; Chen, X.; Jing, P.; Qu, S.; Zhang, L.; Zhou, D.; Zhu, J.; Xu, W.; et al. Doping lanthanide into perovskite nanocrystals: highly improved and expanded optical properties. *Nano Lett.* **2017**, *17* (12), 8005−8011.
(23) Mir, W. J.; Sheikh, T.; Arfin, H.; Xia, Z.; Nag, A. Lanthanide doping in metal halide perovskite nanocrystals: spectral shifting, quantum cutting and optoelectronic applications. *NPG Asia Mater.* **2020**, *12* (1), 1−9.
(24) Jusza, A.; Lipińska, L.; Baran, M.; Olszyna, A.; Jastrzebska, A.; Gil, M.; Mergo, P.; Piramidowicz, R. Praseodymium doped nanocrystals and nanocomposites for application in white light sources. *Opt. Mater.* **2019**, *95*, 109247.
(25) Cybińska, J.; Legendziewicz, J.; Boulon, G.; Bensalah, A.; Meyer, G. Assignment of spectroscopic properties in praseodymium-doped and praseodymium/ytterbium-co-doped ternary K_2LaX_5 (X= Cl, Br, I) Halides. *Opt. Mater.* **2006**, *28* (1−2), 41−52.
(26) Uma, S.; Gopalakrishnan, J. $K_{1-x}La_xCa_{2-x}Nb_3O_{10}$, a layered perovskite series with variable interlayer cation density, and $LaCaNb_3O_{10}$, a novel layered perovskite oxide with no interlayer cations. *J. Solid State Chem.* **1993**, *102* (2), 332−339.
(27) Dieke, G. H.; Crosswhite, H. The spectra of the doubly and triply ionized rare earths. *Appl. Opt.* **1963**, *2* (7), 675−686.
(28) Li, Y.-C.; Chang, Y.-H.; Lin, Y.-F.; Chang, Y.-S.; Lin, Y.-J. Luminescent properties of trivalent praseodymium-doped lanthanum aluminum germanate $LaAlGe_2O_7$. *J. Phys. Chem. Solids* **2007**, *68* (10), 1940−1945.
(29) Kumar, M. K.; Parandamaiah, M.; Babu, Y. C. R.; Kumar, A. S. Spectral studies of praseodymium doped heavy metal borate glass systems. *International Journal Of Engineering And Science* **2014**, 17−24.
(30) Luo, W.; Li, R.; Liu, G.; Antonio, M. R.; Chen, X. Evidence of trivalent europium incorporated in anatase TiO_2 nanocrystals with multiple sites. *J. Phys. Chem. C* **2008**, *112* (28), 10370−10377.
(31) Faustino, B. M.; Foot, P.; Kresinski, R. Synthesis and photoluminescent properties of Sm^{3+}-doped SnO_2 nanoparticles. *Ceram. Int.* **2016**, *42* (16), 18474−18478.
(32) Bouras, K.; Rehspringer, J.-L.; Schmerber, G.; Rinnert, H.; Colis, S.; Ferblantier, G.; Balestrieri, M.; Ihiawakrim, D.; Dinia, A.; Slaoui, A. Optical and structural properties of Nd doped SnO_2 powder fabricated by the sol-gel method. *J. Mater. Chem. C* **2014**, *2* (39), 8235−8243.

(33) Chauhan, I.; Nigam, S.; Sudarsan, V.; Vatsa, R. Hetero-junction assisted improved luminescence of Eu^{3+} doped ZnO-SnO_2 nano-composite. *J. Lumin.* **2016**, *176*, 124−129.
(34) Keller, C. About ternary oxides of niobium and tantalum of the ABO_4 type. *Journal of Inorganic and General Chemistry* **1962**, *318*, 89−106.
(35) Górecka, N.; Szczodrowski, K.; Lazarowska, A.; Barzowska, J.; Michalik, D.; Grinberg, M. The influence of charge compensation defects on the spectroscopic properties of europium doped $Ca_9Y(PO_4)_7$. *RSC Adv.* **2017**, *7* (64), 40549−57.

https://dx.doi.org/10.1021/acsaelm.0c01003
ACS Appl. Electron. Mater. 2021, 3, 461−467